THE EVOLUTION OF SOLAR FLUX FROM 0.1 nm TO 160 μm: QUANTITATIVE ESTIMATES FOR PLANETARY STUDIES

MARK W. CLAIRE[1,2,3], JOHN SHEETS[2,4], MARTIN COHEN[5], IGNASI RIBAS[6], VICTORIA S. MEADOWS[2], AND DAVID C. CATLING[7]

[1] School of Environmental Sciences, University of East Anglia, Norwich, UK NR4 7TJ; M.Claire@uea.ac.uk
[2] Virtual Planetary Laboratory and Department of Astronomy, University of Washington, Box 351580, Seattle, WA 98195, USA
[3] Blue Marble Space Institute of Science, P.O. Box 85561, Seattle, WA 98145-1561, USA
[4] Department of Physics & Astronomy, University of Wyoming, Box 204C, Physical Sciences, Laramie, WY 82070, USA
[5] Radio Astronomy Laboratory, University of California, Berkeley, CA 94720-3411, USA
[6] Institut de Ciències de l'Espai (CSIC-IEEC), Facultat de Ciències, Torre C5 parell, 2a pl, Campus UAB, E-08193 Bellaterra, Spain
[7] Virtual Planetary Laboratory and Department of Earth and Space Sciences, University of Washington, Box 351310, Seattle, WA 98195, USA

ABSTRACT

Understanding changes in the solar flux over geologic time is vital for understanding the evolution of planetary atmospheres because it affects atmospheric escape and chemistry, as well as climate. We describe a numerical parameterization for wavelength-dependent changes to the non-attenuated solar flux appropriate for most times and places in the solar system. We combine data from the Sun and solar analogs to estimate enhanced UV and X-ray fluxes for the young Sun and use standard solar models to estimate changing visible and infrared fluxes. The parameterization, a series of multipliers relative to the modern top of the atmosphere flux at Earth, is valid from 0.1 nm through the infrared, and from 0.6 Gyr through 6.7 Gyr, and is extended from the solar zero-age main sequence to 8.0 Gyr subject to additional uncertainties. The parameterization is applied to a representative modern day flux, providing quantitative estimates of the wavelength dependence of solar flux for paleodates relevant to the evolution of atmospheres in the solar system (or around other G-type stars). We validate the code by Monte Carlo analysis of uncertainties in stellar age and flux, and with comparisons to the solar proxies κ^1 Cet and EK Dra. The model is applied to the computation of photolysis rates on the Archean Earth.

Key words: planets and satellites: atmospheres – stars: solar-type – Sun: evolution – Sun: UV radiation

Online-only material: color figures

1. INTRODUCTION

The Sun has a profound impact on planetary atmospheres. Solar radiation drives such diverse processes as the vertical temperature profile (Fleming et al. 1995), molecular reaction rates (Ribas et al. 2010), and atmospheric escape (Odert et al. 2010). Understanding changes in solar radiation over the age of the solar system is therefore essential to understanding planetary atmospheric evolution (Lean 1997). Our Sun is currently half way through an approximately 10 billion year "middle age" during which, astronomically speaking, nothing dramatic happens. However, as the Sun has aged on the main sequence, the flux in the X-ray and ultraviolet (UV) associated with the magnetically heated upper atmosphere has diminished, while the visible and infrared flux associated with the photosphere has increased by ∼30%. A realistic numerical combination of these trends forms the subject of this paper.

A reliable parameterization of the evolution of solar flux is needed because photochemical models of planetary atmospheres demand knowledge of the solar flux at nanometer resolution through the UV and visible, while climate models are sensitive to changes in visible and infrared fluxes. State-of-the-art photochemical models of early planetary atmospheres have generally either ignored the faint Sun, introduced unphysical step functions to account for enhanced early UV emission (e.g., Kasting et al. 1979; Kasting 1985; Zahnle et al. 2006), or used flux-calibrated spectra from solar proxies to approximate the Sun at a specific age (Segura et al. 2007). The step functions, where large portions of the spectra are simply flat over many tens of nanometers (as shown later in this paper), are highly unrealistic and unnecessary given present astronomical knowledge.

Our goal is to broaden the applicability of recent astronomical data by providing first-order computationally efficient paleoflux estimates applicable at any planet over a broad range of the electromagnetic spectrum and solar ages.

We seek to provide quantitative estimates of the top of the atmosphere solar flux at wavelengths longward of 0.1 nm, at any given time and place in the solar system. Previous work on this topic (Skumanich 1972; Zahnle & Walker 1982; Ayres 1997; Ribas et al. 2005) has illuminated many complicated aspects of the observational and theoretical problem, which we will only briefly describe here while motivating our approach. Numerical parameterizations of solar flux evolution have been applied in recent studies of the atmospheric evolution of Mars, Venus, Titan, and Earth (Lammer et al. 2003; Penz et al. 2005; Kulikov et al. 2006; Lammer et al. 2006; Rybicki 2006; Gillmann et al. 2009; Terada et al. 2009; Manning et al. 2011) but these applications primarily focus on extreme UV and X-ray fluxes, and examine changes in integrated solar energy over wavelength regions of tens to hundreds of nanometers, larger bins than are required by planetary photochemical models.

We construct a series of time and wavelength-dependent "flux multipliers," relative to the modern day flux at the top of Earth's atmosphere. The end result combines four distinct parameterizations that capture the effects of different physics in different solar regimes. First, we use existing observational data to develop broadband flux multipliers for far-UV and shorter wavelengths. Stellar magnetic activity, which drives emission from the upper solar atmosphere, declines with age (Pace & Pasquini 2004), so our short-wave relative flux multipliers start larger than 1 and decrease with stellar age. Second, we use models to create a parameterization based on photospheric
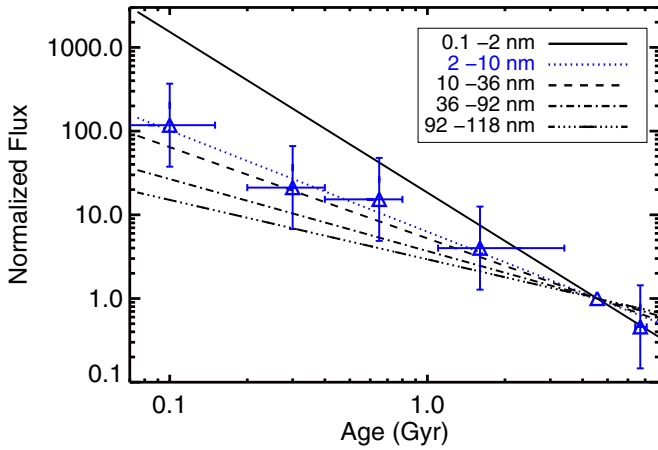
Figure 1. Plots of logarithmic normalized flux vs. logarithmic stellar ages are presented as $F \propto (\tau/4.56\,\mathrm{Gyr})^{\beta}$, with the coefficients determined by fitting astronomical data. This figure is similar to Figure 8 of R05, except that we have subtracted the effect of strong lines from the integrated data. The normalized flux decreases monotonically with increasing wavelengths and with increasing age. This behavior is captured by a monotonic increase of β toward zero at increasing wavelengths. For the 2–10 nm bin, we show the data as (blue) triangles along with our estimations of the uncertainty range in age and flux. Similar uncertainties for all wavelength bins are propagated through a Monte Carlo error analysis in Section 6.1.

(A color version of this figure is available in the online journal.)

Table 1
Power-law Fits to R05 Data without Strong Lines

λ Interval (nm)	α	β
2–10	4.98 ± 0.18	-1.21 ± 0.50
10–36	11.74 ± 0.19	-1.09 ± 0.48
36–92	4.04 ± 0.15	-0.86 ± 0.38
92–118	0.98 ± 0.45	-0.71 ± 0.51

Notes. We fit ($F = \alpha\tau^{\beta}$) the integrated flux data (Table 4 of R05) with the strong line flux (Table 6 of R05) removed. R05 do not provide strong line data within the 2–10 nm bin. Despite using identical data, our fit is slightly different for this bin given that we account for measurement error (our Table 6) within our fit, with resulting large 1σ errors.

fluxes, with flux multipliers increasing (toward 1) with age as a result of hydrogen burning in the solar core (Gough 1981). We present a new analysis of archival data to develop multipliers for the region between 150 and 200 nm that displays both magnetic and photospheric characteristics. Finally, we add in the effects of strong line emission where data are available. These parameterizations are described in Sections 2–4, along with their limitations due to uncertainties about the earliest and future solar rotation rates. The parameterizations are combined via linear weights and applied to high-resolution observations of the flux at the top of Earth's atmosphere in Section 5. Section 6 examines the model uncertainties and checks the results against existing spectral data, while Section 7 discusses ways to extend the parameterizations to varying solar conditions and to the pre-main sequence.

2. MAGNETIC PROCESSES AND SHORT-WAVE FLUXES

Solar short-wave (X-ray and UV) emissions are fundamentally linked to the Sun's evolving magnetic field. The causal relation was first discussed by Skumanich (1972) and is generally referred to as the age–activity–rotation effect. Increasing opacity at shorter wavelengths coupled with a variable solar atmospheric temperature profile conspire to change the character of solar radiation from an absorption line spectrum to emission between (and shortward) of wavelengths between 200 and 150 nm (Vernazza et al. 1981). UV flux and emission lines arise predominantly from the chromosphere, where temperatures increase with height from a minimum of 4500 K near 300 km to ~8000 K around 2200 km (above a surface at 0 km defined as unity optical depth at 500 nm—the "photosphere"). An abrupt temperature rise occurs through the "transition region" (2200–2500 km) to the corona, which is the region above 2500 km with kinetic temperatures near 1 million Kelvin that is responsible for most of the remaining solar short-wave emission. Physical processes in the chromosphere, transition region, and corona are dictated by the solar magnetic field, via complex pathways whose details are still under active debate (Aschwanden et al. 2007; Harvey 2010).

Regardless of the precise mechanism by which the magnetic field dissipates energy in the solar atmosphere, the global picture is relatively well established. The magnetic field, generated deep in the Sun by a rotational dynamo (Parker 1970), couples to the solar wind out to the solar Alfvén radius, approximately 20 Solar radii. This coupling of internal rotational energy to the outer reaches of the stellar atmosphere enables the stellar wind to shed angular momentum over the solar lifetime. The fundamental physics of rotation (which promotes strong magnetic activity and enhanced chromospheric fluxes in young stars) forces stars to spin slower as they age, decreasing their magnetic activity and subsequent short-wave emissivity (Pace & Pasquini 2004).

The evolution of short-wave solar radiation has been the subject of a number of previous investigations, generally motivated by advances in UV and X-ray telescope technology (Skumanich 1972; Zahnle & Walker 1982; Ayres 1997). The most comprehensive study is the "Sun in Time" program, which recently published multi-wavelength results from 20 years of telescopic observation of solar analogs—nearby G stars that are compositionally similar to the Sun but vary in age (Ribas et al. 2005, subsequently referred to as "R05"). Observed fluxes from six solar analogs ranging from 100 Myr through 6.7 Gyr in age were normalized to a distance of 1 AU from a star of 1 solar mass and radius, allowing direct intercomparison. Far-UV and X-ray fluxes were shown to increase for younger Sun-like stars in each wavelength bin studied, with monotonically increasing relative fluxes at shorter wavelengths. Stellar fluxes within integrated wavelength bins were fit via power laws in stellar age, so that flux = $\alpha\tau^{\beta}$, with α and β constants and τ time in Gyr after formation. The power-law exponent β therefore defines the evolution of the flux over the given wavelength range under consideration. Coefficients for wavelength bins between 0.1–2, 2–10, 10–36, 36–92, and 92–118 nm were presented by R05, along with fluxes of and power-law fits to strong emission lines between 28.4 and 165.7 nm. Of these, the strong hydrogen Lyα emission line, which carries up to 50% of the entire modern solar UV flux shortward of 170 nm (R05; Krivova et al. 2006), is the most important for photochemical modeling of planetary atmospheres (e.g. Yung & DeMore 1999). The strong emission lines were included the integrated data used to make the R05 power-law fits. In Figure 1 and Table 1, we show new power-law fits to the R05 data where we explicitly remove the strong line fluxes, along with uncertainty estimates discussed further
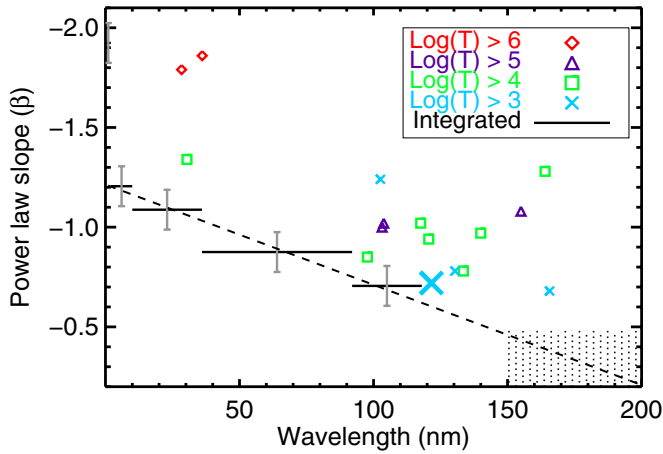
Figure 2. Power-law exponents β vs. wavelength. Values of β measured from individual lines are shown as symbols, labeled by the logarithm of the line formation temperature, T. Line formation temperatures are a proxy for height in the solar atmosphere, with $\log(T) \geqslant 5$ implying line formation in the solar corona. The exponent measured from flux ratios of the Lyα line ($\beta = -0.72$) is shown as an extra-large "x" symbol. Values of β measured from integrated wavelength bins (with strong lines removed) are shown as solid black lines, with the width corresponding to the size of the wavelength bin. R05 estimated the uncertainty in β as ± 0.1 which we indicate as a vertical error bar, and subject to further test in Section 6.1. Equation (1), a fit of β against the R05 wavelength intervals (ignoring 0.1–2 nm), is shown as a dashed line. The vertical hashes between 150 and 200 nm mark the region where we will further enhance the parameterization.

(A color version of this figure is available in the online journal.)

in Section 6.1. To conserve energy, we add the strong lines back to our parameterization in Section 5.1.

Unfortunately for our purpose, R05 do not provide integrated fluxes longward of 120 nm, nor line fluxes longward of 170 nm, due to stated difficulties in separating the chromospheric and photospheric contributions. In the absence of integrated data from 120–200 nm, we extrapolate our results in the following manner. As seen in Figure 1, shorter wavelengths have corresponding higher relative fluxes at earlier times. This behavior corresponds to a monotonic increase in β, the power-law exponent, toward zero with increasing wavelength. The physical basis for this lies in the age–activity–rotation behavior discussed above; as the magnetic heating of the outer atmosphere drops, the high-energy coronal plasma cools faster than the relatively cool plasma responsible for longer wavelength radiation (Ayres 1999). In Figure 2, we plot β versus wavelength with R05's integrated wavelength bins shown as solid lines. We performed a linear fit to the midpoints of the integrated broadband data, subject to the 1σ errors computed in our power-law fits.

The least-squares fit of the power-law exponent β to wavelength λ is given by

$$\beta(\lambda) - 1.21 + \lambda/200, \qquad (1)$$

where λ runs from 2–200 nm, which we take as a maximum wavelength limit for any contribution from the UV/X-ray emission given the changing character of solar radiation from emission to absorption. This fit is plotted as a dashed line in Figure 2. Equation (1) does not pass through R05's data for integrated fluxes from 0.1–2 nm ($\beta = -1.97$), so extrapolations shortward of 2 nm using this fit would underestimate the hard X-ray flux. Our model applies $\beta = -1.97$ to all wavelengths shorter than 2 nm, but we exclude these wavelengths from our error analysis due to limited data. Linear extrapolation of the power-law slopes may slightly under/overestimate the fluxes at

a given line center, but in general conserves energy across the wavelength interval in question. This is justifiable in planetary photochemical models which integrate photons in wavelength bins with resolution of nanometers, but can introduce errors in the unusual case where a species cross section changes drastically over a region of strong line flux, such as occurs with O_2 and the Lyα line (Chabrillat & Kockarts 1997). R05 estimate their errors in each β to be ± 0.1 and state that their approach is sufficient to match observations within 20%. We find computed errors on the fit to each β to be $\sim \pm 0.5$, an estimate we update further in Section 6.1. Exponents that fit measured flux ratios for strong spectral lines are also shown in Figure 2, labeled by the approximate temperature of the solar atmosphere at which the line was generated.

Using Equation (1), we compute relative flux ratios for the far-UV/X-ray as a function of time and wavelength via

$$\text{Flux multiplier}(\tau, \lambda) = \frac{\alpha \tau^{\beta(\lambda)}}{\alpha 4.56^{\beta(\lambda)}} = \left(\frac{\tau}{4.56}\right)^{\beta(\lambda)}, \qquad (2)$$

where the scaling parameters α are given in Table 1, but cancel out here, due to the normalization to the modern Sun. It is important to note that Equation (2) is only one part of a competing set of physical process (including strong lines, photospheric models, and a "chromospheric excess") that will be combined for our final set of flux multipliers between 150 and 200 nm. The dotted areas in Figure 2 and subsequent figures indicate the regions we will enhance further before final combination in Section 5.1. Figure 3(a) is analogous to Figure 1 and displays our extrapolated UV fluxes (relative to modern) versus solar age for various wavelengths. Figure 3(b) displays a portion of our ultimate goal, the UV/X-ray flux multipliers versus wavelength for various solar ages.

One final caveat regards the applicability of this parameterization to the earliest Sun. Observations of young star clusters such as the Pleiades ($\sim$100 Myr; Meynet et al. 1993) reveal that approximately 20% of young stars do not follow the standard age–activity curves, and instead are rotating extremely rapidly (Soderblom et al. 1993a). The presence of these "ultrafast rotators" (UFRs) diminishes as star clusters age, and are absent (Soderblom et al. 1993b) in clusters the age of the Hyades ($\sim$625 Myr; Perryman et al. 1998). Given that G-type stars are born with a wide range of rotational velocities that appear to be funneled down to a rotational period of approximately 10 days by 600 Myr, it is not feasible to predict the exact rotational history of the Sun prior to 600 Myr. The Sun in Time solar analogs are not UFRs and were chosen as representative of the likely rotational evolution for the young Sun, but users of this parameterization for the earliest Sun must be aware of the cautions described above.

3. PHOTOSPHERIC PROCESSES AND THE FAINT YOUNG SUN

We now explore solar photospheric radiation which has an opposite behavior to the short-wave processes modeled above. The photospheric continuum flux arises from the surface layers and lower solar atmosphere where the atoms and radiation are in thermodynamic equilibrium. As hydrogen fuses to form helium in the solar core, the mean molar mass increases, leading to core contraction and increased central temperatures, which increases the rate at which hydrogen is converted to helium. This positive feedback on mass/energy conversion is expressed at the solar surface as an increasing total energy flux over the
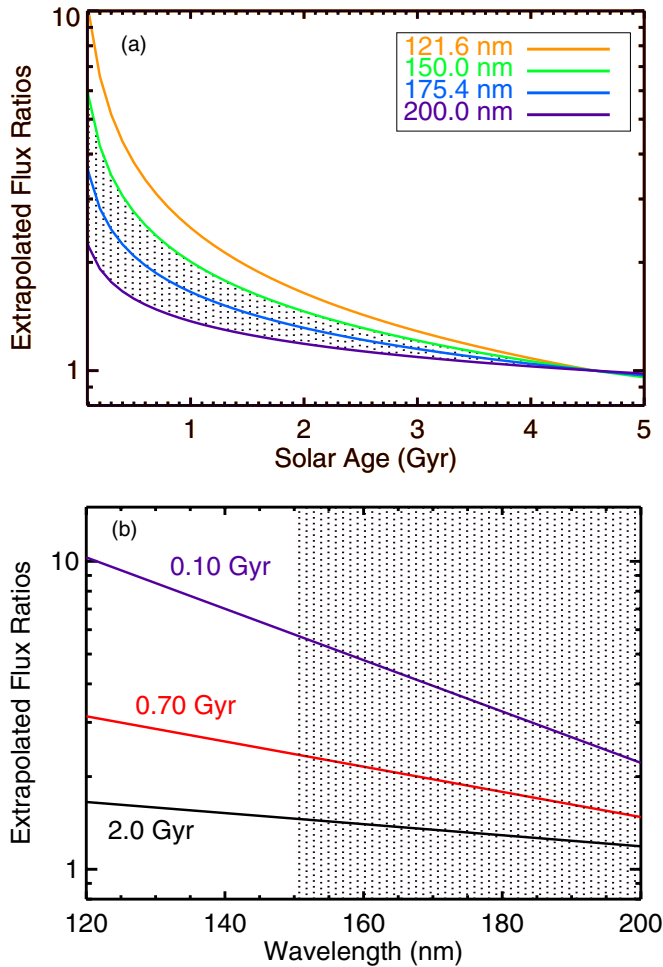
Figure 3. (a) Logarithmic normalized flux ratios vs. solar age, labeled by wavelength. This figure is analogous to Figure 1 except that it is log-linear and also uses the extrapolated $\beta(\lambda)$ relation of Equation (1) to calculate flux ratios at longer wavelengths. Lyα is calculated using the strong line fit $\beta = -0.72$. (b) UV flux ratios vs. wavelength at various paleodates. The vertical hashes between 150 and 200 nm mark the region where we will further enhance the parameterization.

(A color version of this figure is available in the online journal.)

Table 2
Adopted Solar Parameters

Age (Gyr)	Luminosity (Relative)	Radius (Relative)	Effective Temperature (K)	log (g)
0	0.677	0.869	5621	4.560
1	0.764	0.901	5690	4.528
2	0.820	0.924	5719	4.506
3	0.882	0.951	5741	4.481
4	0.954	0.981	5764	4.454
5	1.037	1.016	5784	4.424
6	1.132	1.057	5796	4.390
7	1.235	1.105	5793	4.351
8	1.363	1.166	5781	4.304

Notes. We use cubic splines to interpolate the solar luminosity and radius data of Bahcall et al. (2001). Effective temperature was calculated as $(L/R^2)^{0.25}$ using 5777 K for the present day (Cox 2000) and log (g) was calculated as $4.4377 - \log_{10}(R^2)$.

overshooting ($L/H = 1.25$, where L/H is the ratio of mixing length to scale height). Stellar surface flux moments were extracted from the model atmospheres and converted from frequency to wavelength units in the standard manner.

The flux at Earth, $F_{\rm EARTH}(\tau)$, where τ is the age in Gyr, is computed as

$$F_{\rm EARTH}(\tau) = 4\pi \times F_{\rm MODEL}(\tau) \left(\frac{R(\tau)}{1\,{\rm AU}} \right)^2, \qquad (3)$$

where $F_{\rm MODEL}(\tau)$ is the stellar surface flux per steradian from the Kurucz model (so that $4\pi \times F_{\rm MODEL}(\tau)$ is the stellar surface flux), $R(\tau)$ is the solar radius (Table 2), and 1 AU is the average distance from the Earth to the Sun, assumed constant over the age of the solar system.

Figure 4(a) shows our predictions of solar photospheric flux at Earth for various paleodates. Figure 4(a) illustrates how the luminosity (directly proportional to the integrated flux) increases, and that this increase is driven by enhanced visible radiation near the peak of the blackbody curve. We arrive at Figure 4(b), the relative flux multipliers for the visible and infrared, by dividing the flux curves at a given age by the present day flux. A common zeroth-order correction for the faint young Sun is to multiply the current solar flux by a single factor (75% for the example of 0.7 Gyr) to account for the decrease in bolometric luminosity. Figure 4(b) represents a first-order improvement on this correction by factors ranging up to 2 in the near-UV and a few percent in the visible, the latter of which affects calculations of paleo-temperatures by $\sim$1 °C (Goldblatt et al. 2009). The dotted area in Figure 4(b) indicates where the photospheric parameterization (which predicts lower relative UV for the young Sun) will be combined with the short-wave and chromospheric parameterizations that capture the enhancement in UV due to magnetic activity. Although only displayed on Figure 4 through the visible/near-UV, the Kurucz wavelength grid extends through the far-infrared to 160 μm, so this portion of the parameterization is valid in the IR to the extent that the Kurucz models capture the relevant physics.

4. THE CHROMOSPHERE TO PHOTOSPHERE TRANSITION

Between 150 and 200 nm, the solar spectrum transitions between one dominated by magnetically driven chromospheric emission features and photospheric absorption spectrum arising
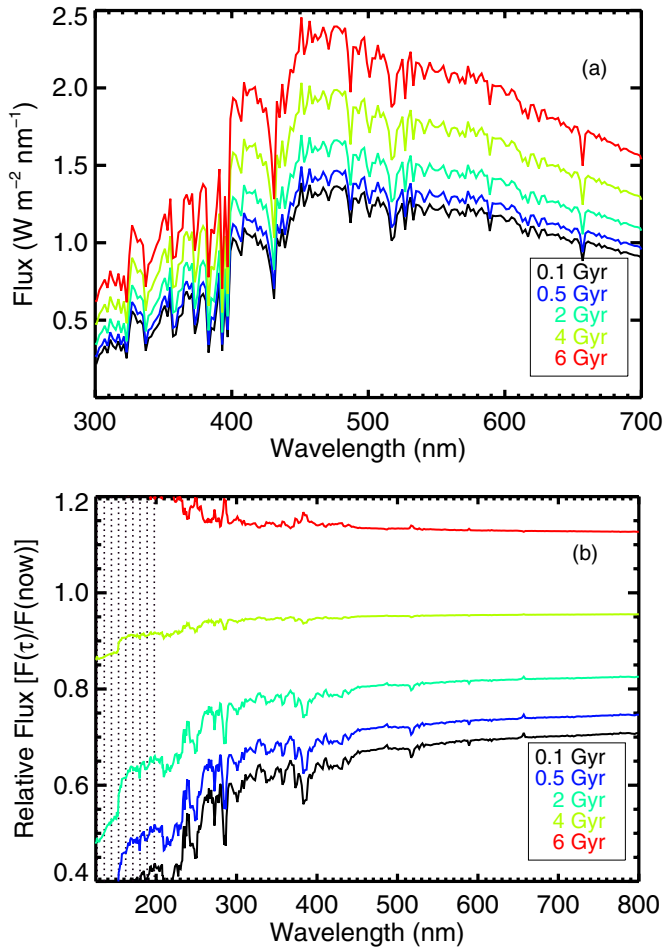
Sun's hydrogen-burning lifetime. The luminosity of the Sun has increased by approximately 30% from the time when the Sun first reached hydrostatic equilibrium on the main sequence (i.e., zero-age main sequence (ZAMS)), to the present (see Table 2). This increasing luminosity leads to the "faint young Sun" problem of atmospheric evolution on the terrestrial planets (Sagan & Mullen 1972; Kasting & Catling 2003), as well as the temporal expansion of the circumstellar habitable zone (Kasting et al. 1993; Rushby et al. 2012).

In order to specify the wavelength dependence of evolving solar photospheric flux, we start with the solar evolution models of Bahcall et al. (2001). First, we interpolate their computed luminosity and radius and calculate effective temperature and surface gravity (Table 2). Next, we use the stellar atmospheric code ATLAS9 (Kurucz 1992; Sbordone et al. 2004) with the updated opacities of Castelli and Kurucz (2003) to predict the solar photospheric flux along the Sun's evolutionary path. We compute a grid of 43 Kurucz model atmospheres (at solar ages of 0.0, 0.1, 0.2, 0.3–7.9 in 0.2 Gyr steps, and 8.0 Gyr), fixing solar metallicity (Grevesse & Sauval 1998), microturbulence velocity (2 km/s), and pure mixing-length convection without

Figure 4. (a) Kurucz model fluxes at 1 AU for the photospheric age/effective temperature/log (*g*) relations described in Table 2. (b) Kurucz model flux ratios at 1 AU vs. age and wavelength in the visible and near-IR. The vertical hashes between 150 and 200 nm mark the region where we will further enhance the parameterization.

(A color version of this figure is available in the online journal.)

Figure 5. (a) Observed flux from κ^1 Cet (solid line) and best-fit Kurucz model (dashed line), using the parameters in Table 3. Both spectra are normalized to 1 AU. (b) Fits of power-law exponent vs. wavelength for the excess flux from the chromosphere (plus symbols, Table 5) along with a third-order polynomial fit given by Equation (4).

(A color version of this figure is available in the online journal.)

lower in the atmosphere. The R05 integrated results formally extend to 120 nm, which we extrapolated to 200 nm in Figure 2 and Equation (1). R05 mention that the reason for the cutoff of their integrated results (and strong-line data at 170 nm) was the difficulty in accounting for the continuum contribution. This is fully consistent with detailed physical models that show the last major chromospheric absorption edge at 168.1 nm (Vernazza et al. 1981). In order to account for the increasing photospheric activity underlying the magnetic activity in this portion of the solar spectra, we use archival data to perform a new analysis following the general methodology of R05. Using the same six solar analogs, we compile the "chromospheric excess" flux due solely to chromospheric activity and construct power-law fits in age for each wavelength interval. Following the methodology described in Section 2, we then fit our calculated power-law indices against wavelength to isolate the time and wavelength dependence of the chromospheric excess flux.

We constructed stellar energy distributions for the solar analog stars from the UV through the IR following the method described by Segura et al. (2003). For each star, the observed near- and far-UV spectra from *IUE* were carefully combined and the results merged with synthetic stellar photospheric spectra (Castelli & Kurucz 2003) computed using the stellar parameters
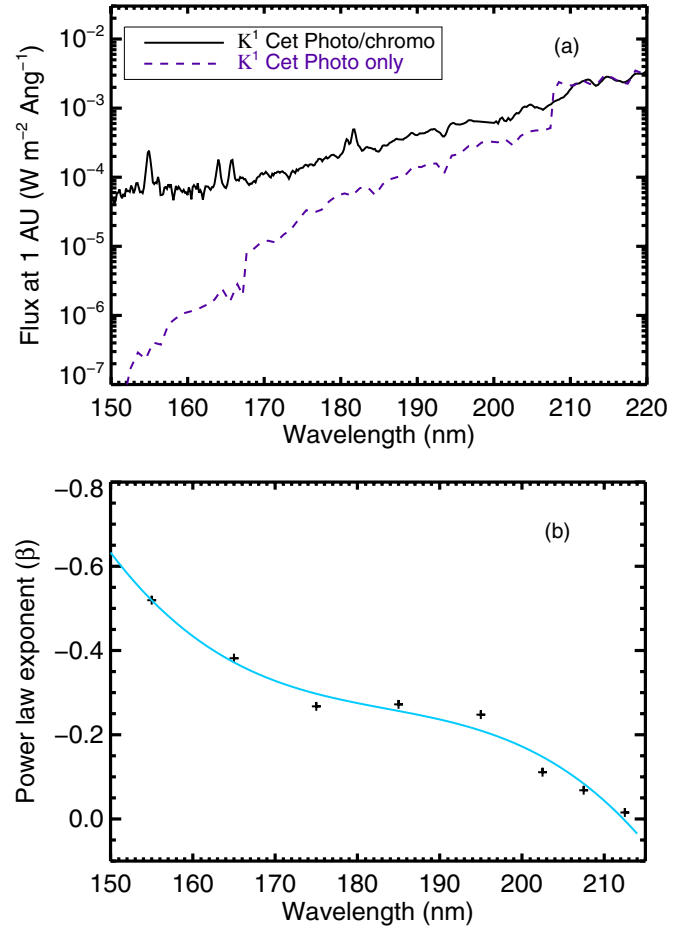
in Table 3. We then normalized the photospheric spectra using all available UV, optical, and IR photometry.

The merge was made at the aluminum absorption edge at 208 nm in each star, and representative spectra for κ^1 Cet are shown in Figure 5(a). We integrate the empirical data (containing photospheric and chromospheric contributions) and the photospheric spectrum of each star and divide to define the "chromospheric excess" emission associated with solar analogs of different ages (Table 4).

As with the R05 data, the relative fluxes are larger (for a given star) at shorter wavelengths and can be well approximated by power laws (in flux versus age) for a given wavelength bin. Table 5 and Figure 5(b) show coefficients for power-law fits for each wavelength bin. Similar to Equation (1) and Figure 2, we fit the power-law exponents as a function of wavelength via

$$\beta_{\mathrm{CHROMO}}(\lambda) = 6.55 \times 10^{-6}\lambda^3 - 3.61 \times 10^{-3}\lambda^2$$
$$+ 6.65 \times 10^{-1}\lambda - 41.43. \quad (4)$$

$\beta_{\mathrm{CHROMO}}(\lambda)$ is valid from 150 to 210 nm and is shown in Figure 5(b). We adopted a third-order polynomial fit for Equation (4) and Figure 5(b), although note that chi-square goodness-of-fit tests support both a linear and a third-order polynomial fit, depending on the chosen error model. We define the chromospheric excess flux as a function of solar age by

Table 3
Adopted Stellar Parameters

Solar Proxy	HD Alias	Effective Temperature (K)	log (g)	[Fe/H]	R05 Age (Gyr)	Adopted Age Range (Gyr)
EK Dra	129333	5765	4.61	−0.04	0.1	0.02–0.15 a,b
π^1 Uma	72905	5821	4.54	−0.07	0.3	0.2–0.4 c,d
χ^1 Ori	39587	5964	4.68	−0.12	0.3	0.2–0.4 c,d
κ^1 Cet	20630	5742	4.49	+0.10	0.65	0.4–0.8 d,e
β Com	114710	6075	4.57	−0.04	1.6	1.1–3.6 c,d,f
β Hyi	2151	5784	4.04	−0.023	6.7	6.4–7.1 g

Notes. Fundamental stellar parameters were taken from the literature after critical comparisons of derived parameters, notably effective temperatures, from SPOCS (Valenti & Fischer 2005), S4N (Prieto et al. 2004), the NASA Star and Exoplanet Database (NStED, no longer in operation), the Nearby Stars Database Project at NAU (http://nstars.nau.edu/nau_nstars/about.htm), the STELIB3 library of stellar spectra (Le Borgne et al. 2003), and the STELIB5 online update (http://webast.ast-mip.fr/stelib). References for the adopted age ranges in our Monte Carlo study are: a, Montes et al. (2001); b, Jarvinen et al. (2007); c, Barnes (2007); d, Mamajek & Hillenbrand (2008); e, Ribas et al. (2010); f, Lachaume et al. (1999); g, Fernandes & Monteiro (2003).

Table 4
Excess Flux due to Chromospheric Activity

λ Interval (nm)	0.10 Gyr (EK Dra)	0.30 Gyr (π^1UMa + χ^1 Ori)	0.65 Gyr (κ^1 Cet)	1.6 Gyr (β Com)	4.56 Gyr (Sun)	6.7 Gyr (β Hyi)
150–160	332.26	90.98	202.69	62.48	25.31	57.46
160–170	48.54	18.57	29.71	15.84	8.40	12.40
170–180	8.73	4.24	5.94	3.76	3.30	2.55
180–190	6.39	3.23	4.36	2.17	2.80	1.72
190–200	4.22	2.18	2.09	1.70	2.22	1.32
200–205	3.13	2.09	2.65	1.81	2.40	1.61
205–210	1.08	1.21	1.14	0.98	1.10	0.67
210–215	1.27	1.19	1.19	1.25	1.30	1.06

Notes. The ratio of wavelength-integrated measured flux to photospheric flux. The total uncertainty in measurement and combination varies from 10% to less than 1% as a function of wavelength. This error, along with error due to intrinsic stellar variability, is discussed in Section 6.1.

Table 5
Power-law Fits to Chromospheric Activity

λ Interval (nm)	α	β
150–160	94.61 ± 32.55	−0.52 ± 0.17
160–170	18.76 ± 3.55	−0.38 ± 0.10
170–180	4.37 ± 0.50	−0.27 ± 0.07
180–190	3.14 ± 0.40	−0.27 ± 0.07
190–200	2.12 ± 0.26	−0.25 ± 0.07
200–205	2.25 ± 0.18	−0.11 ± 0.05
205–210	1.02 ± 0.07	−0.07 ± 0.05
210–215	1.21 ± 0.03	−0.01 ± 0.01

Note. Power-law fits to the relative flux data in Table 4.

substituting Equation (4) into Equation (2). The chromospheric excess flux is not a flux multiplier as previously defined. Rather, it was constructed to reflect only the portion of the solar flux that is not due to photospheric processes. As such, we subtract 1 from the chromospheric excess flux (so that it equals zero when there is no contribution from the chromosphere) and add it to the photospheric flux multiplier to form a combined photosphere + chromosphere flux multiplier between 150 and 210 nm. The chromospheric and photosphere + chromosphere multipliers are shown in Figure 6.

5. THE EVOLUTION OF SOLAR FLUX

5.1. Combining the Parameterizations

We combine the four parameterizations of UV/X-ray without strong lines, strong line emission, chromospheric excess, and photospheric fluxes. Figure 6 combines Figures 2, 3(b), 4(b), and 5(b) and shows our relative flux multipliers, first as separate short-wave, chromospheric, and photospheric components (Figure 6(a)). Figure 6(b) combines the parameterizations by a linear weighting of the short-wave and photosphere + chromosphere parameterizations between 150 and 170 nm. Also included in the combined parameterization are the strong line fluxes from Figure 2, added in 0.2 nm bins. Figure 6(b) is a graphical representation of our goal, a parametric representation of relative flux multipliers for a given wavelength at a given paleodate, along with previous efforts shown for comparison. Note the extreme crudeness of previous parameterizations used in terrestrial atmospheric chemistry models and how we have improved upon those estimates.

5.2. The Modern Solar Flux

A parameterization of relative flux multipliers allows freedom of choice for the specification of the modern-day flux. For the general purposes considered here, we choose to use the Solar Irradiance Reference Spectra normalized to the multiwavelength ATLAS 1 observations, which were obtained near the peak of a sunspot cycle (Thuillier et al. 2003; Thuillier
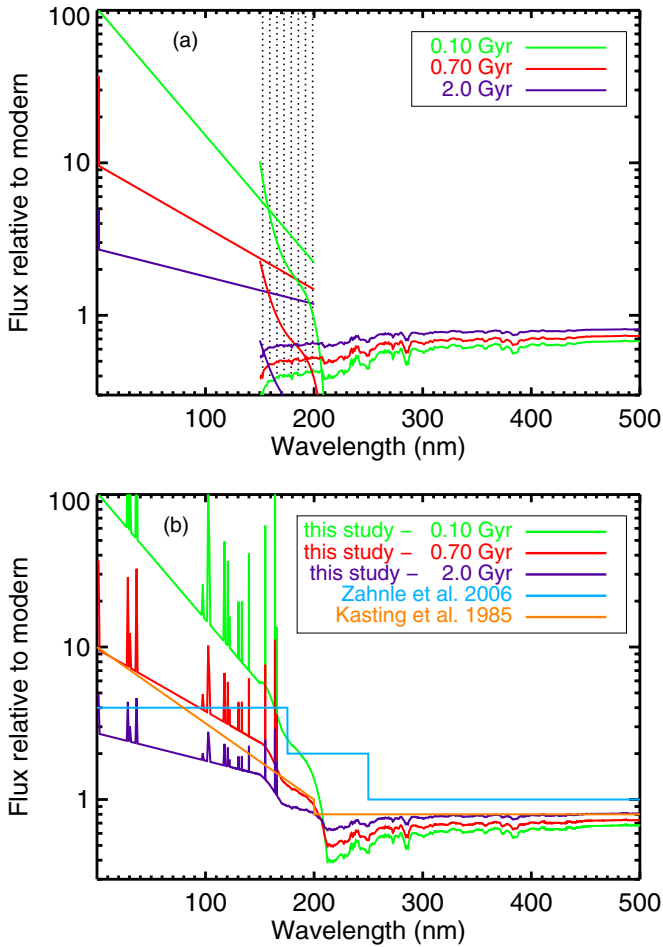
Figure 6. (a) Flux ratios at 1 AU by wavelength for the 0.1, 0.7, and 2.0 Gyr Sun—for X-ray/UV, chromospheric excess, and photospheric processes, separately. The vertical hashes between 150 and 200 nm mark the region where we will further enhance the parameterization. $\beta = -1.92$ behavior for 0.1–2 nm can be seen at the far left of the figure. (b) Flux ratios at 1 AU from panel (a) combined via a linear weighting of the short wave with the photospheric plus chromospheric parameterizations between 150 and 170 nm. Strong line flux ratios from R05 (shown in Figure 2) are added in 0.2 nm bins, except for Lyα which was added as a 1.6 nm bin. Our parameterizations are nominally valid from 0.1 to 16,000 nm and for main-sequence evolution from 0.6 to 6.7 Gyr, with extensions from 0 to 8 Gyr subject to additional caveats discussed in the text. Previous parameterizations from the photochemical models of Kasting (1985) and Zahnle et al. (2006) are shown for comparison.

(A color version of this figure is available in the online journal.)

et al. 2004). We chose a solar maximum spectrum for our reference because many lines that provide significant paleoflux are negligible at solar minimum (R05). Utilizing the R05 fits ensures that we capture the total integrated flux in our shortest wavelengths bins, even if specific lines pertinent to the early Sun are not present in the modern spectrum.

Thuillier et al. (2004) present solar spectra from 0.5 to 2400 nm in units of mW m^{-2} nm^{-1} (i.e., spectral irradiance). For photochemical modeling, it is common to use units of photons cm^{-2} s^{-1} nm^{-1} (i.e., actinic flux). The conversion from the energy units of irradiance to the quantized units of actinic flux is made via

$$
\begin{aligned}
\text{Actinic Flux} &= \frac{10^{-7} \times \text{Irradiance}}{E_\lambda} \\
&= 5.039 \times 10^8 \ \text{Irradiance} \times \lambda,
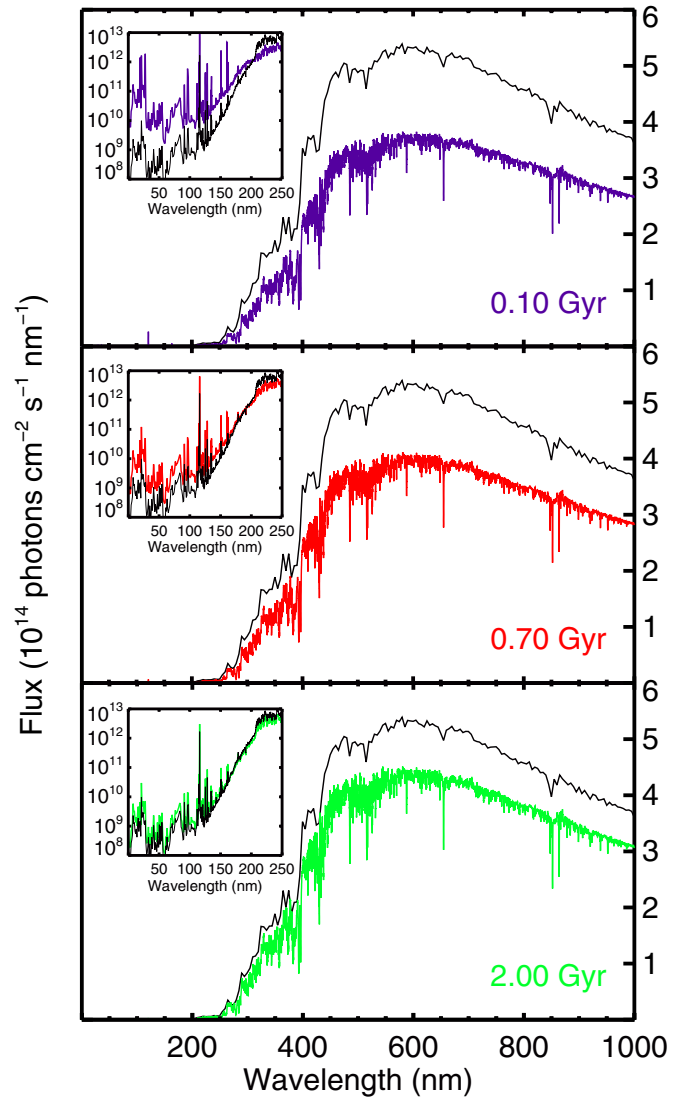\end{aligned} \tag{5}
$$

Figure 7. Predicted flux at Earth vs. wavelength for the 0.1, 0.7, and 2.0 Gyr Sun. Each panel displays a high-resolution thick-lined trace of flux for the given paleodate, along with a thin-lined modern flux trace binned at 2 nm resolution for comparison. In each panel, the visible portion of the flux is displayed linearly in units of 10^{14} photons cm^{-2} s^{-1} nm^{-1} and is mapped to the right side axes. The inset of each subplot shows the UV region of the spectrum, displaying logarithmic flux (from 10^8 to 10^{13} photons cm^{-2} s^{-1} nm^{-1}) vs. wavelength from 10 to 250 nm.

(A color version of this figure is available in the online journal.)

where 10^{-7} converts mW m^{-2} to W cm^{-2}, E_λ is the energy per photon in Joules ($E_\lambda = 1.98468 \times 10^{-16}/\lambda$), and λ is wavelength measured in nanometers.

5.3. The Evolution of Solar Flux

Figure 7 shows our relative flux multipliers applied to a representative modern-day solar flux in energy units, and subsequently converted to quantized units. The solar actinic fluxes at 0.1, 0.7, and 2.0 Gyr are shown as they compare to the modern-day (4.56 Gyr) flux, with insets showing the emission-line behavior in the UV.

6. VERIFICATION

We first performed simple tests of integrated flux in various wavelength regions. Using energy units for the flux, we find that

Table 6
Uncertainty Estimates

Wavelength Regime (nm)	Instrument	Measurement Error (%)	Solar Intrinsic Variability (%)
2–10	*ROSAT*	20	193
10–36	*EUVE*		106
28.4, 30.4, 36.1		20	199, 53, 126
36–92	Interpolated[a]	50	99
92–118	*FUSE*		72
97.7, 102.6, 103.2, 103.8, 117.6		10	145, 112, 115, 100, 55
121.6	*HST*/MAMA	28[b]	63
120.6, 130.4, 133.5, 140.0, 155.0, 164.0, 165.7, 150–160, 160–170, 170–180, 180–190, 190–200, 200–210, 210–215	*IUE*	3 (strong lines) Between 10–1 otherwise	78, 24, 53, 60, 31, 16, 12, 21, 13, 9, 10, 7, 6, 4

Notes. Uncertainty estimates for instrumental error and in the intrinsic variability adopted for the solar proxies.
[a] According to R05, these inferred fluxes are interpolations based upon the observed solar flux and the power-law relationship. This method could be flawed if strong emission lines are present within this interval, although solar spectra reveal only relatively weak lines of He I, Mg X, O V, O VI, O II, and C III. Nevertheless, we assume a large "measurement" error for this interval.
[b] This is a combination of an estimated 8% error for the photometric accuracy of the *HST* STIS MAMA echelle spectrograph, plus an additional 20% uncertainty due to systematic uncertainties in astrospheric corrections (Wood et al. 2005).

the integrated contribution from wavelengths less than 400 nm to the total flux was approximately constant at ∼8% throughout stellar evolution, while the integrated contribution from wavelengths shorter than 200 nm decreases by a factor of 10 (0.1% to 0.01%) from the ZAMS to the present, consistent with declining chromospheric activity. The fractional contribution of the Lyα line to the entire flux shortward of 170 nm increases from ∼20% for the early Sun to approximately 36.5% in the ATLAS 1 normalized spectrum of Thuillier et al. (2004). When using quantized units (i.e., actinic flux) we find that the relative fraction of Lyα photons with respect to all photons less than 170 nm remains approximately 40% from the ZAMS to the present. These fractions are consistent with previous estimates in R05, but are not entirely independent.

In order to further validate the parameterization, we performed a Monte Carlo analysis to explore the effect of uncertainty in the data (Section 6.1). In Sections 6.2 and 6.3, we compare our predictions to astronomical measurements from two young solar analogs, κ^1 Cet and EK Dra.

6.1. Uncertainty in the Parameterization

The three primary sources of uncertainty in the data are the unknown age of the solar proxies, primary measurement errors, and the intrinsic variability of the solar proxies. To quantify these uncertainties, we ran Monte Carlo simulations that varied both the adopted stellar ages and the primary flux data within the limits described below.

6.1.1. Solar Proxy Ages

As with most stars besides the Sun, the solar proxies have uncertain ages. We surveyed the literature for age estimates for each star and adopted the ranges shown in Table 3. In order to form an upper bound on the age uncertainty, we gave no preference to the mechanism used to determine ages, and simply compiled the oldest and youngest published proxy age estimates.

6.1.2. Measurement Errors

Many factors could influence the R05 observational data, such as noise attributable to stellar fluctuations, sky background,

and/or detector imperfections. To account for this, we randomized the primary flux data in each iteration of our Monte Carlo simulation using telescopic uncertainty estimates compiled in Table 6.

6.1.3. Intrinsic Variability

In all likelihood, the solar proxies have sunspot cycles somewhat similar to that of the Sun. While the solar data in R05 are representative of the average Sun, the data from the solar proxies may have been collected anywhere in between their respective minima or maxima.

Lacking a uniform set of variability data for the proxies, we compiled data on solar variability (Woods & Rottman 2002; Woods et al. 2005; Krivova et al. 2006; Domingo et al. 2009; Table 6), which we apply to the proxies using an age-dependent correction. While younger stars are more active, they are more consistently active and therefore less variable than the Sun. This occurs because sunspots provide a lower relative contrast difference on an actively flaring surface than on a more quiescent surface (Gudel & Telleschi 2007; Favata et al. 2008). For example, the X-ray variability of EK Dra over its rotational cycle is a factor of 2.4 (Gudel et al. 2001). The Sun varies by a factor of ∼10 at 2 nm to a factor of 2 at 10 nm, with an average factor near 3 (recorded as 193% in Table 6). EK Dra's X-ray variability is therefore between 0.8 and 0.24 that of the Sun's. We adopt a wavelength-independent value of 0.4 for EK Dra and assume a linear increase in variability with time so that

$$\text{Variability Factor } (\tau) = 0.4 + 0.13 \times \tau. \qquad (6)$$

For example, the 103.2 nm O VI line varies by 115% over the solar cycle. In our simulation of this line strength in the other stars, we assume a 10% *FUSE* measurement error combined with 115% × 0.413 = 48% variability in EK Dra and 115% × 1.33 = 153% intrinsic variability for β Hyi.

6.1.4. Monte Carlo Simulation

In each iteration, we select a random age for each stellar proxy (but not the Sun) from within the age ranges in Table 3. Then we randomly select values for both measurement error and age-scaled intrinsic variability, and use a multiplicative method to

assign new flux values from within the uncertainty ranges. The randomized flux and stellar ages were used to calculate power-law fits for each wavelength interval, and the resulting power-law exponents were then fit against wavelength in a method analogous to that in Figures 2 and 5(b). A similar process was done separately for each strong emission line for which R05 reported data from at least three stars, and for the chromospheric fits. We exclude errors in Kurucz model spectra (∼2%) from our analyses.

Figures 8(a) and (b) display the averaged results from 5000 iterations of a 0.06 Gyr Sun. The variance in our model decreases with stellar age, so these represent an upper limit to the influence of primary data uncertainty on our model fits. Figure 8(a) shows the Monte Carlo spread of power-law exponents versus wavelength for the short-wave parameterization, along with our original β and fit given by Equation (1). The mean fits to β are 0.1–0.2 lower than our original values, indicating that the uncertainty due to intrinsic variability, stellar age, and measurement error cause us to, in general, overestimate flux power-law dispersions in each wavelength bin. This leads to a potential overestimate of our fit, Equation (1), although we note that the slopes of our original fit and to the Monte Carlo mean values are similar. Figure 8(b) compiles the average percent error (the difference between the randomized data and the standard model divided by the standard model) as a function of wavelength for 5000 iterations of a 0.06 Gyr Sun and further illuminates this general trend. Compared to our standard model, the average model fluxes as a function of wavelength are ∼35% lower shortward of 150 nm, except at the position of strong lines. The kinks in the uncertainty at 150 and 170 nm are where the chromospheric parameterization overlaps with the short-wave and photosphere parameterizations, respectively. The mean Lyα line flux was 9% higher than our standard model, highlighting the need for additional studies on this important line in solar proxies. In Figure 8(c), we show the mean and absolute mean wavelength-integrated uncertainty as a function of solar age.

6.1.5. Uncertainty Analysis Notes and Discussion

Figure 8(c) illustrates the overall uncertainty inherent in our model. It encompasses errors due to fundamental parameters along with our choice of fitting functions. The average deviation between the randomized and standard model resultant fluxes decays from a maximum absolute error of 25% to 0% for the modern Sun. Therefore, at its worst (the 0.06 Gyr Sun), our integrated model results are accurate to within ∼25% of their reported flux values, considering the uncertainties described above. When sign is accounted for, the mean error is generally biased to lower values, but is never less than ∼20% for any stellar age. Taken as a whole, these results confirm our model as viable for making paleoflux estimates, with a maximum error of 25% at the youngest solar age investigated, dropping to ∼10% by the start of Earth's Archean eon (0.76 Gyr). These uncertainties could be reduced by further studies into the variability cycles of these solar proxies and by increasing precision in stellar age estimates.

6.2. Comparison with Stellar Data: κ^1 Cet

κ^1 Cet is young solar analog from the Sun in Time data set, but its precise age is unknown. While R05 estimate κ^1 Cet at 0.65 Gyr, a follow-up study (Ribas et al. 2010) provides age estimates from 0.4 to 0.8 Gyr using equally robust methodologies. In order to test our predictions for the young Sun, we compile multiple wavelength
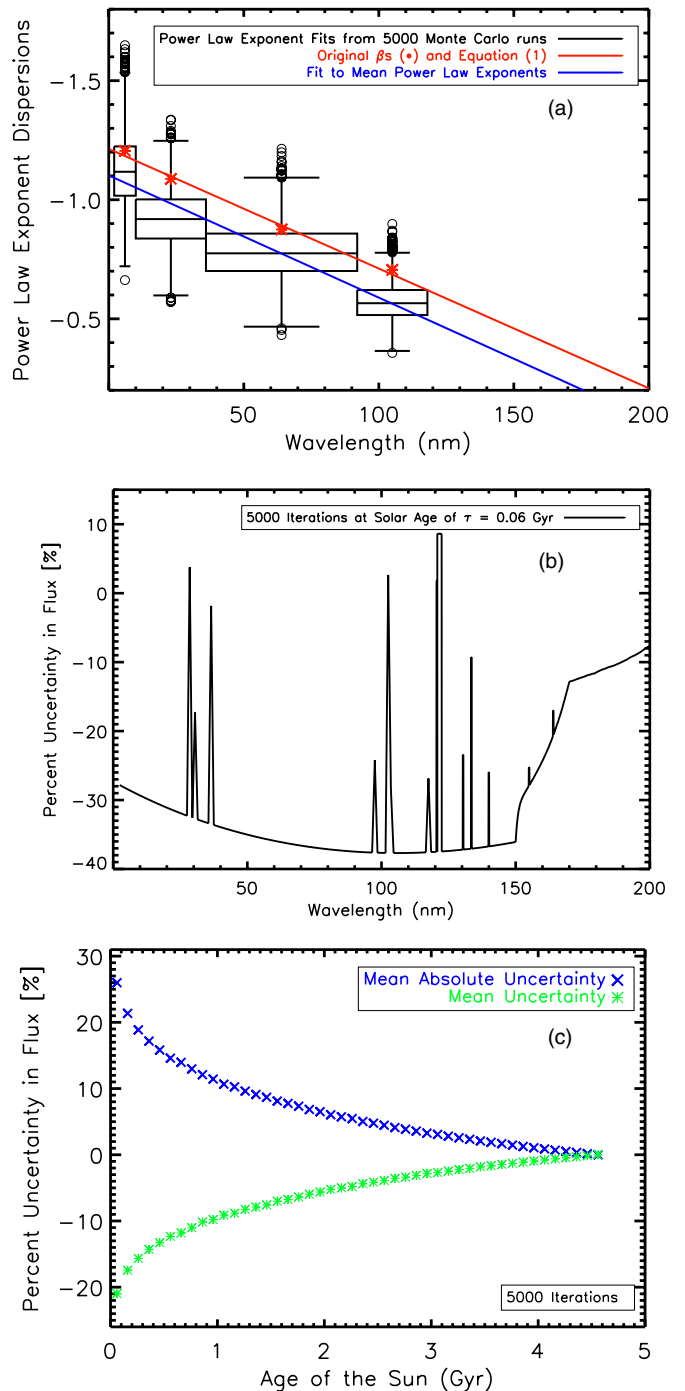

Figure 8. (a) Distribution of power-law exponents from 5000 iterations of our Monte Carlo simulation for the youngest Sun (0.06 Gyr, when our model inaccuracy is likely to be highest). The central horizontal lines in each box represent the median power-law exponent, while the top and bottom of the boxes represent the interquartile range (IQR) or the data's 75th and 25th quartile, respectively. The whiskers extend to 1.5 times the IQR above and below the top and the bottom of the boxes, respectively. Outlier exponents are plotted as circles. (b) For 5000 iterations of a 0.06 Gyr Sun, the wavelength-dependent uncertainty from our Monte Carlo model. The data are presented as percent error (the difference between randomized flux and the standard flux, divided by the standard flux) and are averaged over 5000 iterations. Our model is most uncertain at this young solar age, so this figure represents an upper limit to our wavelength-dependent uncertainty. (c) For each of the 46 stellar ages plotted, the (green) asterisks are the wavelength-integrated mean uncertainty, while the (blue) × are the wavelength-integrated absolute uncertainties, both reported as percent error.

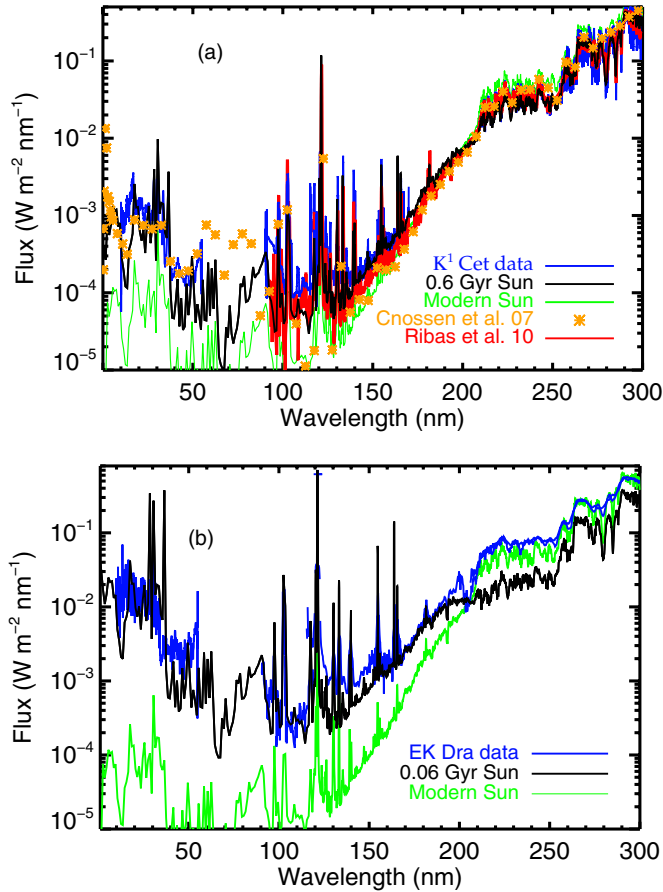(A color version of this figure is available in the online journal.)

Figure 9. (a) Comparison of model predictions to available data for κ^1 Cet. Data, shown as a (blue) line, are from *EUVE* (10–70 nm), *FUSE* (90–119 nm), and *HST*-STIS (120–300 nm). The high-resolution spectral flux (at top of Earth's atmosphere) for the Sun at 0.6 Gyr from this study is shown as a thick black solid line, with the modern solar flux shown for comparison as a thin green solid line. The Cnossen et al. (2007) modeled flux at 1 AU from κ^1 Cet is shown as (orange) "∗" symbols (Cnossen et al. 2007). (b) EK Dra data are shown as (blue) "+" symbols and are taken from *EUVE* (10–70 nm), *FUSE* (90–119 nm), and Segura et al. (2007; 115–300 nm). The Sun at 0.1 Gyr as predicted by this study is shown as a thick black solid line, with the modern Sun shown for comparison as a thin gray solid line.

(A color version of this figure is available in the online journal.)

spectral data for κ^1 Cet from the *Extreme-Ultraviolet Explorer* (*EUVE*; via MAST Archive—http://archive.stsci.edu/), *FUSE* (S. Engle 2008, private communication), and the *Hubble Space Telescope* (*HST*) Imaging Spectrograph (via CoolCAT—http://casa.colorado.edu/~ayres/CoolCAT). The *FUSE* data are uncorrected for solar contamination and hence contain added geocoronal emission in the Lyman series (92–97.3 nm) and O VI lines (103.2–103.7 nm; E. Guinan 2008, private communication). These data are compiled in Figure 9(a), along with our predictions for the Sun at 0.6 Gyr, which overlies the κ^1 Cet raw and smoothed (Ribas et al. 2010) data very well. For comparative purposes, Figure 9(a) also shows a recently modeled low-resolution spectrum for κ^1 Cet by Cnossen et al. (2007). This spectrum, created via spectral synthesis of emission measure estimations, matches the data well from 2 to 60 nm and longward of 200 nm, but is consistently lower than the data throughout most of the far-UV and Lyman continuum, a region which is difficult to model given lack of observational constraints. Also overplotted in Figure 9(a) is the modern solar spectrum, which appears to fit the Cnossen et al. (2007)

model well in this region, although this is likely coincidental. Overall, our predictions represent an improvement on existing models and are surprisingly accurate given the simplicity of the methodology.

6.3. Comparisons with Stellar Data: EK Dra

Our parameterization has increased uncertainty for stars younger than 0.6 Gyr given the previously discussed rotational funneling effect that effectively homogenizes the spin down rate of G stars. EK Dra is a member of the Pleiades moving group and hence ~100 Myr old (Meynet et al. 1993). Like κ^1 Cet, it was a member of the Sun in Time program, so we would expect our parameterization to fit it fairly well, at least at the strong lines. Figure 9(b) shows available data for EK Dra from *EUVE*, *FUSE*, and the UV spectrum of Segura et al. (2007), which was taken from existing *IUE* data and models of observational data in the visible. No empirical measurement exists for this star's Lyα flux and the existing low-resolution *IUE* data are compromised by geocoronal emission. We have followed Segura et al. (2007) in adopting the R05 estimate for the EK Dra Lyα flux. Strong lines for which we do not have data are apparent in Figure 9, which motivates additional temporal studies of lines such as He I (58.4, 108.5 nm), Mg X (61, 62.5 nm), the He II series (92.7–97.2 nm), S VI (93.3, 94.4 nm), and N III (99.1 nm). The effective temperature of EK Dra is 5765 K (Segura et al. 2007), directly comparable to the modern Sun, while the Bahcall et al. (2001) prediction for the Sun at 0.1 Gyr is 5645 K (Table 2), leading to a significant discrepancy in the photospheric region longward of 170 nm. It is important to note that EK Dra is a solar analog but not a solar twin, and may not be representative of the Sun's photospheric flux at 0.1 Gyr. Near-UV observations of young G stars with cooler effective temperatures would help illuminate this problem (Dorren & Guinan 1994) and are worthy of future effort given the relevance to the faint young Sun problem.

7. DISCUSSION

We have constructed a numerical parameterization for modifications to solar flux as a function of solar age and wavelength. Specifically, we have considered enhancements in UV and X-ray flux due to enhanced magnetic activity and decreases in visible and infrared flux due to lower energy generation rates, and estimated our uncertainties as a function of stellar age. The flux at other solar system objects is found by dividing $F_{\text{EARTH}}(\tau)$ by the square of the distance of the object from the Sun measured in AU.

We have discussed changes to the Sun's flux over its main-sequence lifetime, but the solar flux also varies on shorter timescales ranging from seconds (flares) to decades (radio flux) to millennia (Earth's orbital variations; Lean 1997). The methodology of relative flux multipliers could be extended to account for other physical processes by construction of suitable functions normalized to representative conditions. Examples include seasonal changes in Sun–planet distance (Spencer 1971), or evolution of solar activity over a sunspot cycle (Lean et al. 2001; Harder et al. 2009; Fontenla et al. 2011). The fluxes displayed in Figure 7 were chosen as representative of the Sun near the peak of a sunspot cycle. Our methodology is applicable to any measurement of top-of-atmosphere flux, and so could be applied to fluxes measured at varying solar conditions and/or flare events, as a means of estimating flux variations of these events at various paleodates. In addition, the parameterizations
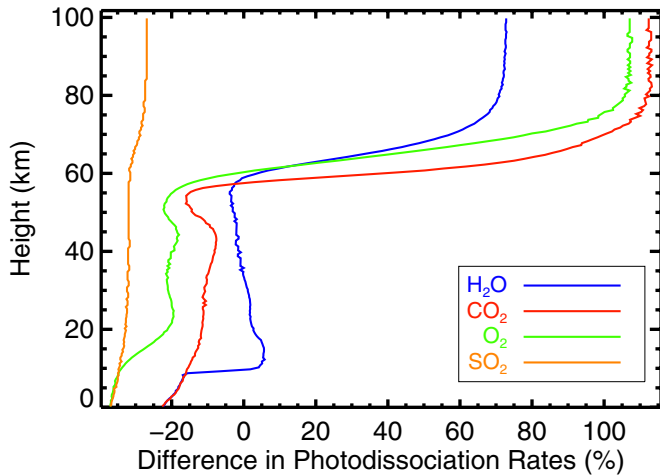
Figure 10. Change [(Archean rates − Modern rates)/Modern rates] in photolysis rate constants (s^{-1}) computed in two one-dimensional Archean photochemical model runs. The model runs differed only in the top of the atmosphere solar flux, with one using the modern solar flux and the other using the solar flux from 3 billion years ago as predicted by our model.

(A color version of this figure is available in the online journal.)

provided are valid for studies of the future evolution of the Sun, at least to ∼6.7 Gyr (the R05 age of β Com). If the flux ratios calculated by R05 can be extrapolated in time an extra Gyr, the parameterization is nominally valid until 8 Gyr (the limit of our fits to photospheric luminosity and radius).

These parameterizations provide a reasonable first-order approximation to the solar flux at various paleodates, but they are far from perfect. Nonetheless, approximate corrections for the faint Sun and magnetic activity are necessary improvements bearing in mind the crude schemes implemented by published models of evolving planetary atmospheres. The quantitative flux predictions should be integrated over nanometer-sized bins rather than being considered detailed predictions of flux at the sub-angstrom scale. Future enhancements include the addition of additional strong lines in the far-UV (e.g., He I, He II, N III), strong lines in the near-UV (e.g., Mg II, Fe II, Ca II), and better understanding of the Lyman continuum.

We have presented the first model of paleoflux in the complicated spectral region between 120 and 300 nm. The region from 190 to 290 nm is of particular interest to photochemical modelers of Earth's early atmosphere, as these photons reached the lower atmosphere in the absence of substantial atmospheric ozone (Kasting & Donahue 1980; Cnossen et al. 2007). In particular, mass-independent fractionation in sulfur isotopes has been attributed to changes in photon optical depth in this wavelength region (Farquhar et al. 2000; Pavlov & Kasting 2002; Domagal-Goldman et al. 2008; Ueno et al. 2009; Claire & Kasting 2010) and so there are observable geochemical consequences. To illustrate this, we ran one-dimensional photochemical models for the (reducing) Archean atmosphere (Zahnle et al. 2006; Domagal-Goldman et al. 2011; Zerkle et al. 2012) using the modern solar flux and a solar flux at 1.56 Gyr (3.0 billion years ago). The resulting change in photolysis rates of some key atmospheric species are shown in Figure 10 and are in excess of the intrinsic uncertainty in the paleoflux estimates. Photolysis rates (and therefore the details of atmospheric composition) are therefore sensitive to the choice of solar flux used, which strongly motivates the adoption of our model in studies of planetary atmospheres.

8. CONCLUSIONS

We have described how to compute wavelength-dependent scaling factors for solar flux anywhere in the solar system from 0.6 to 6.7 Gyr. With additional care, the parameterization is valid from 0 to 8 Gyr. These first-order parameterizations are valid from 0.1 nm through the infrared. Interactive Data Language (IDL) and FORTRAN codes that calculate relative flux multipliers, as well as estimated solar spectra are available upon request to the first author and via the Virtual Planetary Laboratory Web site at http://depts.washington.edu/naivpl/content/models/solarflux/.

REFERENCES

Aschwanden, M. J., Winebarger, A., Tsiklauri, D., & Peter, H. 2007, ApJ, 659, 1673
Ayres, T. R. 1997, J. Geophys. Res., 102, 1641
Ayres, T. R. 1999, ApJ, 525, 240
Bahcall, J. N., Pinsonneault, M. H., & Basu, S. 2001, ApJ, 555, 990
Barnes, S. A. 2007, ApJ, 669, 1167
Castelli, F., & Kurucz, R. L. 2003, in IAU Symp. 210, Modelling of Stellar Atmospheres, ed. N. E. Piskunov, W. W. Weiss, & D. F. Gray (Uppsala: ASP), A20
Chabrillat, S., & Kockarts, G. 1997, Geophys. Res. Lett., 24, 2659
Claire, M. W., & Kasting, J. F. 2010, Geochim. Cosmochim. Acta, 74, A181
Cnossen, I., Sanz-Forcada, J., Favata, F., et al. 2007, J. Geophys. Res., 112, E02008
Cox, A. N. 2000, Allen's Astrophysical Quantities (New York: Springer)
Domagal-Goldman, S., Johnston, D., Farquhar, J., & Kasting, J. F. 2008, Earth Planet. Sci. Lett., 269, 29
Domagal-Goldman, S., Meadows, V. S., Claire, M. W., & Kasting, J. F. 2011, Astrobiology, 11, 29
Domingo, V., Ermolli, I., Fox, P., et al. 2009, Space Sci. Rev., 145, 337
Dorren, J. D., & Guinan, E. F. 1994, ApJ, 428, 805
Farquhar, J., Bao, H., & Thiemans, M. 2000, Science, 289, 756
Favata, F., Micela, G., Orlando, S., et al. 2008, A&A, 490, 1121
Fernandes, J., & Monteiro, M. J. P. F. G. 2003, A&A, 399, 243
Fleming, E. L., Chandra, S., Jackman, C. H., et al. 1995, J. Atmos. Terr. Phys., 57, 333
Fontenla, J. M., Harder, J., Livingston, W., Snow, M., & Woods, T. 2011, J. Geophys. Res., 116, D20108

Gillmann, C., Chassefiere, E., & Lognonne, P. 2009, Earth Planet. Sci. Lett., 286, 503

Goldblatt, C., Claire, M. W., Lenton, T. M., et al. 2009, Nature Geosci., 2, 891

Gough, D. O. 1981, Sol. Phys., 74, 21

Grevesse, N., & Sauval, A. J. 1998, Space Sci. Rev., 85, 161

Gudel, M., Audard, M., Smith, K., et al. 2001, in 12th Cambridge Workshop on Cool Stars, Stellar Systems, and the Sun, The Future of Cool-Star Astrophysics, ed. A. Brown, G. M. Harper, & T. R. Ayres (Boulder: Univ. Colorado Press), 303

Gudel, M., & Telleschi, A. 2007, A&A, 474, L25

Harder, J. W., Fontenla, J. M., Pilewskie, P., Richard, E. C., & Woods, T. N. 2009, Geophys. Res. Lett., 36, L07801

Harvey, J. W. 2010, Space Sci. Rev., 12

Jarvinen, S. P., Berdyugina, S. V., Korhonen, H., et al. 2007, A&A, 472, 887

Kasting, J. F. 1985, The Carbon Cycle and Atmospheric CO2: Natural Variations Archean to Present, ed. E. T. Sundquist & W. S. Broecker (Washington DC: American Geophysical Union), 612

Kasting, J. F., & Catling, D. 2003, ARA&A, 41, 429

Kasting, J. F., & Donahue, T. M. 1980, J. Geophys. Res., 85, 3255–3263

Kasting, J. F., Liu, S. C., & Donahue, T. M. 1979, J. Geophys. Res., 84, 3097

Kasting, J. F., Whitmire, D. P., & Reynolds, R. T. 1993, Icarus, 101, 108

Krivova, N. A., Solanki, S. K., & Floyd, L. 2006, A&A, 452, 631

Kulikov, Y. N., Lammer, H., Lichtenegger, H. I. M., et al. 2006, Space Sci. Rev., 129, 207

Kurucz, R. L. 1992, in IAU Symp. 149, Stellar Population of Galaxies, ed. B. Barbuy & A. Renzini (Angra dos Reis: Kluwer), 225

Lachaume, R., Dominik, C., Lanz, T., & Habing, H. J. 1999, A&A, 348, 897

Lammer, H., Kulikov, Y. N., & Lichtenegger, H. I. M. 2006, Space Sci. Rev., 122, 189

Lammer, H., Lichtenegger, H. I. M., Kolb, C., et al. 2003, Icarus, 165, 9

Lean, J. 1997, ARA&A, 35, 33

Lean, J. L., White, O. R., Livingston, W. C., & Picone, J. M. 2001, J. Geophys. Res., 106, 10645

Le Borgne, J. F., Bruzual, G., Pello, R., et al. 2003, A&A, 402, 433

Mamajek, E. E., & Hillenbrand, L. A. 2008, ApJ, 687, 1264

Manning, C. V., Ma, Y. J., Brain, D. A., et al. 2011, Icarus, 212, 131

Meynet, G., Mermilliod, J. C., & Maeder, A. 1993, A&AS, 98, 477

Montes, D., Lopez-Santiago, J., Fernandez-Figueroa, M. J., & Galves, M. C. 2001, A&A, 379, 976

Odert, P., Leitzinger, M., Hanslmeier, A., et al. 2010, Int. J. Astrobiol., 9, 239

Pace, G., & Pasquini, L. 2004, A&A, 426, 1021

Parker, E. N. 1970, ApJ, 162, 665

Pavlov, A. A., & Kasting, J. F. 2002, Astrobiology, 2, 27

Penz, T., Lammer, H., Kulikov, Y. N., & Biernat, H. K. 2005, Adv. Space Res., 36, 241

Perryman, M. A. C., Brown, A. G. A., Lebreton, Y., et al. 1998, A&A, 331, 81

Prieto, C. A., Barklem, P. S., Lambert, D. L., & Cunha, K. 2004, A&A, 420, 183

Ribas, I., de Mello, G. F. P., Ferreira, L. D., et al. 2010, ApJ, 714, 384

Ribas, I., Guinan, E. F., Gudel, M., & Audard, M. 2005, ApJ, 622, 680

Rushby, A., Claire, M., Osborn, H., & Watson, A. 2012, Astrobiology, submitted

Rybicki, K. R. 2006, PASP, 118, 1124

Sagan, C., & Mullen, G. 1972, Science, 177, 52

Sbordone, L., Bonifacio, P., Castelli, F., & Kurucz, R. L. 2004, Mem. Soc. Astron. Ital. Suppl., 5, 93

Segura, A., Krelove, K., Kastings, J. F., et al. 2003, Astrobiology, 3, 689

Segura, A., Meadows, V. S., Kasting, J. F., et al. 2007, A&A, 472, 665

Skumanich, A. 1972, ApJ, 171, 565

Soderblom, D. R., Stauffer, J. R., Hudon, J. D., & Jones, B. F. 1993a, ApJS, 85, 315

Soderblom, D. R., Stauffer, J. R., Macgregor, K. B., & Jones, B. F. 1993b, ApJ, 409, 624

Spencer, J. W. 1971, Search, 2, 172

Terada, N., Kulikov, Y. N., Lammer, H., et al. 2009, Astrobiology, 9, 55

Thuillier, G., Floyd, L., Woods, T. N., et al. 2004, in Solar Variability and Its Effects on Climate, ed. J. M. Pap & P. Fox (Washington, DC: American Geophysical Union), 256

Thuillier, G., Herse, M., Labs, D., et al. 2003, Sol. Phys., 214, 1

Ueno, Y., Johnson, M. S., Danielache, S. O., et al. 2009, Proc. Natl Acad. Sci., 106, 14784

Valenti, J. A., & Fischer, D. A. 2005, ApJS, 159, 141

Vernazza, J. E., Avrett, E. H., & Loeser, R. 1981, ApJ, 45, 635

Wood, B. E., Redfield, S., Linsky, J. L., et al. 2005, ApJS, 159, 118

Woods, T., & Rottman, G. 2002, in Comparative Aeronomy in the Solar System, ed. M. Mendillo, A. Nagy, & J. Hunter-Waite, Jr. (Geophys. Monograph Series, Vol. 130; Washington, DC: American Geophysical Union), 221

Woods, T. N., Eparvier, F. G., Bailey, S. M., et al. 2005, J. Geophys. Res., 110, A01312

Yung, Y. L., & DeMore, W. B. 1999, Photochemistry of Planetary Atmospheres (New York: Oxford Univ. Press)

Zahnle, K. J., Claire, M. W., & Catling, D. C. 2006, Geobiology, 4, 271

Zahnle, K. J., & Walker, J. C. G. 1982, Rev. Geophys. Space Phys., 20, 280

Zerkle, A. L., Claire, M., Domagal-Goldman, S. D., et al. 2012, Nature Geosci., 5, 359